Plasmonics (2015) 10:569–583
DOI 10.1007/s11468-014-9842-9

Topology Optimization-Based Computational Design Methodology for Surface Plasmon Polaritons

Yongbo Deng · Zhenyu Liu · Chao Song · Junfeng Wu · Yongshun Liu · Yihui Wu

Received: 19 September 2014 / Accepted: 5 November 2014 / Published online: 22 November 2014

Abstract This paper presents the topology optimization-based computational design methodology for nanostructures in surface plasmon polaritons. Using the proposed method, nanostructures can be designed solely based on the user's desired performance specification for the surface plasmon polaritons. This topology optimization-based computational design methodology is implemented based on the material interpolation with hybrid formulation of logarithmic and power law approaches, to mimic the metal surface with exponential decay of the electromagnetic field. The constructed computational design problem is analyzed using the continuous adjoint method, and the filter and projection techniques are utilized to ensure the minimum length scale in the obtained nanostructures. The outlined design methodology is used to investigate the nanostructures for localized surface plasmonic resonances, extraordinary optical transmission, and surface plasmonic cloaking, respectively. For localized surface plasmonic resonances and extraordinary optical transmission, the metallic nanostructures are designed with spectra peaks at the prescribed wavelengths and the shift of the spectra peak is controlled by solving the computational design problem corresponding to a different incident wavelength; for surface plasmonic cloaking, the cloak covered at a curved metal-dielectric interface is designed to bound the surface plasmon polariton at the interface and remove the radiation, where the conventional simple isotropic dielectric readily available in nature is used instead of the material possessing gradient electromagnetic properties with challenges on realization for optical frequencies.

Keywords Topology optimization · Surface plasmon polaritons · Localized surface plasmonic resonances · Extraordinary optical transmission · Surface plasmonic cloaking

Introduction

Surface plasmon polaritons (SPPs) are electromagnetic waves trapped at the interface between a metal with a negative real part and a dielectric with a positive real part of the permittivity [1, 2]. The metals used for SPPs are usually noble metals, e.g., silver and gold. At optical frequencies, the metal's free electrons can sustain, under certain conditions, oscillations with distinct resonance frequencies [3–5]. The existence of surface plasmons is characteristic for the interaction between metal and light, where the Kretschmann-Raether and Otto configurations are commonly used for plasmon excitation.

Many innovative concepts of SPPs have been developed over the past few years, e.g., localized surface plasmon resonances (LSPRs) [7], extraordinary optical transmission (EOT) [6], and transformational plasmon optics [8, 9]. Correspondingly, many related applications have also been proposed for SPPs, e.g., biomolecular manipulation and labeling [10], surface-enhanced Raman spectroscopy (SERS) [11], chemical and biological sensors [12], photo-voltaics [13], near-field lithography and imaging [14], optical

---

Y. Deng (✉) · C. Song · J. Wu · Y. Liu · Y. Wu
State Key Laboratory of Applied Optics Changchun Institute of Optics, Fine Mechanics and Physics (CIOMP),
Chinese Academy of Sciences, Changchun, 130033 China
e-mail: yongbo_deng@hotmail.com

Z. Liu
Changchun Institute of Optics, Fine Mechanics and Physics (CIOMP), Chinese Academy of Sciences, Changchun,
130033 China

trapping [15, 16], nano-optic circuits [17], opto-electronic devices, wavelength-tunable filters, optical modulators [18–21], plasmonic Luneburg lens, and surface plasmonic cloaking [8, 9]. All these applications utilize surface plasmonic effects by reasonably designing the nano-scale structures. For the design of surface plasmonic devices, transformational plasmon optics has been developed to determine the refractive index distribution and guide the SPP propagation [8, 9]. However, the derived distribution has extreme electromagnetic properties, i.e., permittivity and permeability, which are achieved based on the use of metamaterials. The tailored microstructure of such metamaterials has to be much smaller than the wavelength, and this makes it very challenging to realize the desired magnetic properties for optical frequencies. To overcome the similar problems in bulk optical waves and use the conventional simple isotropic dielectric readily available in nature, topology optimization-based computational design method has been used to implement the inverse design of cloak for bulk optical wave [22–24]. On surface plasmons, most related researches are focused on designing nanostructures by tuning a handful of structural parameters [25–27], although the topology optimization method has been applied for the grating couplers to enhance the excitation efficiency of surface plasmons [28]. Therefore, it is still deficient on the systematic research of full-parameter computational design of nanostructures for SPPs.

Topology optimization is a full-parameter method used to inversely determine the distribution of materials [29]. In contrast to designing devices by tuning a handful of structural parameters, topology optimization method utilizes the full-parameter space to design structures solely based on the user's desired performance specification. Therefore, topology optimization can inversely find the reasonable shape and topology, simultaneously, and it is a more general computational design methodology than shape optimization, which usually improves the performance of a device by adjusting the positions of structural boundaries, keeping the topology of the structure unchanged. And topology optimization has been extended to multiple physical problems, such as acoustic, electromagnetic, fluidic, optical, thermal, and material design problems [30–42]. Therefore, topology optimization is chosen to develop the computational design methodology for SPPs.

This paper is organized as follows: the topology optimization-based computational design methodology is stated in "Methodology" section; by specifying the desired functionality and performance of the SPP nanostructures, several results are obtained in "Results and Discussion" section for localized surface plasmon resonances, extraordinary optical transmission, and surface plasmonic cloaking (SP cloaking), respectively, and the paper is concluded in "Conclusion" section. All the mathematical descriptions are carried out using Cartesian coordinate system in the following sections.

Methodology

Modeling

This paper is focused on the two-dimensional (2D) SPP problems. In 2D modeling case, SPPs are excited by TM (magnetic field in the z direction) polarized waves, scattered by metallic nanostructures. For TM waves propagating in the $x-y$ plane, the scattered-field formulation is used in order to reduce the dispersion error

$$\nabla \cdot \left[\epsilon_r^{-1} \nabla \left(H_{zs} + H_{zi}\right)\right] + k_0^2 \mu_r \left(H_{zs} + H_{zi}\right) = 0, \text{ in } \Omega \quad (1)$$

where $H_z = H_{zs} + H_{zi}$ is the total field, H_{zs} and H_{zi} are the scattered and incident fields, respectively; ϵ_r and μ_r are the relative permittivity and permeability, respectively; $k_0 = \omega\sqrt{\epsilon_0 \mu_0}$ is the free space wave number with ω, ϵ_0, and μ_0 representing the angular frequency, free space permittivity, and permeability, respectively; Ω is the computational domain; the time dependence of the fields is given by the factor $e^{j\omega t}$, with t representing the time. The incident field can be obtained by solving the electromagnetic equations in free space, with boundary conditions representing realistic working conditions.

The boundary conditions of Eq. 1 usually include the first-order absorbing condition, periodic boundary condition, and symmetric condition. The first-order absorbing condition is usually used to truncate the field distribution at infinity [44]

$$\epsilon_r^{-1} \nabla H_{sz} \cdot \mathbf{n} + j k_0 \sqrt{\epsilon_r^{-1} \mu_r} H_{sz} = 0, \text{ on } \Gamma_{ab} \quad (2)$$

where j is the imaginary unit; $\mathbf{n}$ is the unit outward normal vector at the boundary $\partial\Omega$ of the computational domain; Γ_{ab} is the absorbing boundary included in $\partial\Omega$. Periodicity of nanostructures plays a crucial role in tuning the optical response, and single nanostructure can be approximated by the periodic case with low volume ratio of the nanostructure. Therefore, the periodic boundary condition for the scattered field, induced by the periodic incident wave, is often imposed on the piecewise pair included in $\partial\Omega$

$$\begin{aligned} &H_{sz}(\mathbf{x}+\mathbf{a}) = H_{sz}(\mathbf{x}), \\ &\mathbf{n}(\mathbf{x}+\mathbf{a}) \cdot \nabla H_{sz}(\mathbf{x}+\mathbf{a}) = -\mathbf{n}(\mathbf{x}) \cdot \nabla H_{sz}(\mathbf{x}), \\ &\text{for } \forall \mathbf{x} \in \Gamma_{ps}, \ \mathbf{x}+\mathbf{a} \in \Gamma_{pd} \end{aligned} \quad (3)$$

where Γ_{pd} and Γ_{ps} composes one piecewise periodic boundary pair, with Γ_{pd} and Γ_{ps}, respectively, being the destination and source boundaries; **a** is the lattice vector of the periodic nanostructures. The symmetry of the incident wave and material distribution gives rise to the symmetrical characteristic of the scattered field. Then the symmetric condition can be used to reduce the computational cost and ensure the computational accuracy effectively

$$\epsilon_r^{-1}\nabla H_{sz}\cdot\mathbf{n}=0,\ \text{on}\ \Gamma_{sm} \tag{4}$$

where Γ_{sm} is the symmetric boundary included in $\partial\Omega$.

The topology optimization-based computational design of SPP nanostructure is implemented based on the material interpolation between two different materials. In the design with the requirement to commonly determine the structural topology of metal and dielectric, e.g., the design of nanostructures for LSPRs and EOT, the material interpolation should be implemented between metal and dielectric. Meanwhile, the material interpolation should be implemented between two different dielectrics (or between dielectric and free space) for the design of dielectric nanostructures adjoined to the metal with fixed configuration, e.g., the design of SP cloak. In SPPs, the used noble metal is usually nonmagnetic. Therefore, the relative permeability μ_r is set to be 1. Then, only the spatial distribution of relative permittivity is varied iteratively in the evolution of the design variable representing the structural topology. In this research, the design variable is filtered by the Helmholtz filters [43, 45] to ensure the distribution smoothness and numerical stability, where the Helmholtz filters are implemented by solving the following Helmholtz equations

$$\begin{aligned}-r^2\nabla\cdot\nabla\rho_f+\rho_f &= \rho,\ \text{in}\ \Omega\\ \nabla\rho_f\cdot\mathbf{n} &= 0,\ \text{on}\ \partial\Omega\end{aligned} \tag{5}$$

where r is the filter radius chosen based on numerical experiments [45]; $\rho\in[0,1]$ is the design variable; ρ_f is the filtered design variable. To ensure the minimum length scale and remove the gray area in the obtained structural topology, the filtered design variable is projected by the threshold method [46–48]

$$\rho_{fp}\left(\rho_f\right)=\frac{\tanh\left(\beta\xi\right)+\tanh\left(\beta\left(\rho_f-\xi\right)\right)}{\tanh\left(\beta\xi\right)+\tanh\left(\beta\left(1-\xi\right)\right)} \tag{6}$$

where ρ_{fp} is the projected design variable called physical density which takes the place of the design variable to represent the structural topology [48]; $\xi\in[0,1]$ and β are the threshold and projection parameters for the threshold projection, respectively. On the choice of the values of ξ and β, one can refer to [46, 49]. Then, the physical density ρ_{fp} is utilized to interpolate the relative permittivity between two different materials corresponding to $\rho_{fp}=0$ and $\rho_{fp}=1$, respectively. For surface plasmons at the metal-dielectric interface, the electromagnetic field decays exponentially; hence, the material interpolation should decays rapidly away from interface to mimic the metal surface. Therefore, the material interpolation is implemented in the hybrid of logarithmic and power law approaches [50]

$$\epsilon_r\left(\omega\right)=10^{\log\epsilon_{rm}\left(\omega\right)-\frac{1-\rho_{fp}^3}{1+\rho_{fp}^3}\left[\log\epsilon_{rm}\left(\omega\right)-\log\epsilon_{rd}\left(\omega\right)\right]} \tag{7}$$

where ϵ_{rm} and ϵ_{rd} are the relative permittivity of metal and dielectric (or free space), respectively. If the structural topology is determined between two dielectrics adjoined to the metal with fixed configuration, one only need to change the relative permittivity ϵ_{rm} in Eq. 7 to be that of one dielectric. In the visible light region, the relative permittivity of noble metals can be described by the Drude model

$$\epsilon_{rm}\left(\omega\right)=\epsilon_{r\infty}-\frac{\omega_p^2}{\omega\left(\omega-j\gamma_c\right)} \tag{8}$$

where $\epsilon_{r\infty}$ is the high-frequency bulk permittivity; ω is the angular frequency of the incident wave; ω_p is the bulk plasmon frequency; γ_c is the collision frequency. The values of the parameters in Eq. 8 can be obtained by fitting the experimental data in the literature [51].

Based on the above description, the variational problem for the topology optimization-based computational design of 2D SPP nanostructures can be formulated as

$$\begin{aligned}&\text{Find}\ \rho\\ &\text{minimize or maximize}\ J\left(H_{zs},\nabla H_{zs},\rho_{fp};\rho\right)\\ &\text{Subject to}\ \begin{cases}\nabla\cdot\epsilon_r^{-1}\nabla\left(H_{zs}+H_{zi}\right)\\ \qquad+k_0^2\mu_r\left(H_{zs}+H_{zi}\right)=0,\ \text{in}\ \Omega\\ -r^2\nabla\cdot\nabla\rho_f+\rho_f=\rho,\ \text{in}\ \Omega\\ 0\le\rho\le1,\ \text{in}\ \Omega\end{cases}\end{aligned} \tag{9}$$

where the Helmholtz filter equation is included in the partial differential equation constraints. J is the generally formulated design objective, which include both the domain and boundary integrations about the unknowns

$$\begin{aligned}J\left(H_{zs},\nabla H_{zs},\rho_{fp};\rho\right)=&\int_\Omega A\left(H_{zs},\nabla H_{zs},\rho_{fp};\rho\right)\,\mathrm{d}\Omega\\ &+\int_{\partial\Omega}B\left(H_{zs}\right)\,\mathrm{d}\partial\Omega\end{aligned} \tag{10}$$

where A and B are integral functionals chosen based on the mathematical description of the desired performance of SPPs.

Analyzing

In this section, the variational problem for computational design is analyzed to obtain the gradient information used to iteratively evolve the design variable. According to [52–54], the adjoint method is an efficient approach to derive the derivative of the objective in the partial differential equation constrained variational problem. Then, the adjoint equations of Eqs. 1 and 6 are obtained using the Lagrangian multiplier-based adjoint method (see Appendix for more details)

$$\begin{aligned}
&\nabla \cdot \left(\epsilon_r^{-1} \nabla \tilde{H}_{zs}^*\right) + k_0^2 \mu_r \tilde{H}_{zs}^* = -\frac{\partial A}{\partial H_{zs}} + \nabla \cdot \frac{\partial A}{\partial \nabla H_{zs}}, \text{ in } \Omega \\
&\epsilon_r^{-1} \nabla \tilde{H}_{zs}^* \cdot \mathbf{n} + j k_0 \sqrt{\epsilon_r^{-1} \mu_r}\, \tilde{H}_{zs}^* = \frac{\partial A}{\partial \nabla H_{zs}} \cdot \mathbf{n} + \frac{\partial B}{\partial H_{zs}}, \text{ on } \Gamma_{ab} \\
&\epsilon_r^{-1} \nabla \tilde{H}_{zs}^* \cdot \mathbf{n} = \frac{\partial A}{\partial \nabla H_{zs}} \cdot \mathbf{n} + \frac{\partial B}{\partial H_{zs}}, \text{ on } \Gamma_{pd} \cup \Gamma_{ps} \cup \Gamma_{sm}
\end{aligned} \tag{11}$$

and

$$\begin{aligned}
-r^2 \nabla^2 \tilde{\rho}_f^* + \tilde{\rho}_f^* &= \frac{\partial \epsilon_r^{-1}}{\partial \rho_{fp}} \frac{\partial \rho_{fp}}{\partial \rho_f} \nabla \left(H_{zs} + H_{zi}\right) \cdot \nabla \tilde{H}_{zs}^* \\
&\quad - \frac{\partial A}{\partial \rho_{fp}} \frac{\partial \rho_{fp}}{\partial \rho_f}, \text{ in } \Omega \\
r^2 \nabla \tilde{\rho}_f^* \cdot \mathbf{n} &= j k_0 \frac{\partial \sqrt{\epsilon_r^{-1}}}{\partial \rho_{fp}} \frac{\partial \rho_{fp}}{\partial \rho_f} \sqrt{\mu_r} H_{zs} \tilde{H}_{zs}^* \\
&\quad - \frac{\partial \epsilon_r^{-1}}{\partial \rho_{fp}} \frac{\partial \rho_{fp}}{\partial \rho_f} \nabla H_{zi} \cdot \mathbf{n} \tilde{H}_{zs}^*, \text{ on } \Gamma_{ab} \\
r^2 \nabla \tilde{\rho}_f^* \cdot \mathbf{n} &= -\frac{\partial \epsilon_r^{-1}}{\partial \rho_{fp}} \frac{\partial \rho_{fp}}{\partial \rho_f} \nabla H_{zi} \cdot \mathbf{n} \tilde{H}_{zs}^*, \\
&\quad \text{on } \Gamma_{pd} \cup \Gamma_{ps} \cup \Gamma_{sm}
\end{aligned} \tag{12}$$

where $\tilde{H}_{zs} \in \mathcal{H}^{1*}(\Omega)$ and $\tilde{\rho}_f \in \mathcal{H}^{1*}(\Omega)$ are the adjoint variables of the state variables $H_{zs} \in \mathcal{H}^1(\Omega)$ and $\rho_f \in \mathcal{H}^1(\Omega)$, respectively; $\mathcal{H}^1(\Omega)$ is the first-order Sobolev space, and $\mathcal{H}^{1*}(\Omega)$ is the dual space of $\mathcal{H}^1(\Omega)$; for complex, $*$ represents the conjugate operation. It is valuable to notice that $\tilde{H}_{zs}^*$ and ρ_f^* are more convenient to be solved than $\tilde{H}_{zs}$ and ρ_f in the adjoint Eqs. 11 and 12. Therefore, the adjoint Eqs. 11 and 12 are utilized to solve $\tilde{H}_{zs}^*$ and ρ_f^*, and $\tilde{H}_{zs}$ and ρ_f can be obtained using conjugate operation. The adjoint derivative of the computational design problem is obtained as (see Appendix for more details)

$$\tfrac{\delta \hat{J}}{\delta \rho} = \Re\left(\tfrac{\partial A}{\partial \rho} - \tilde{\rho}_f^*\right), \text{ in } \Omega \tag{13}$$

where ρ is valued in $\mathcal{L}_2(\Omega)$, the second-order Lebesgue integrable functional space; $\Re(\cdot)$ is the real part of an expression. In Eq. 13, only the real part of the adjoint derivative is utilized because the design variable ρ is the distribution defined on real space. In engineering, the variational problem for computational design may need to be regularized furthermore by some integral constraints, e.g., constraint of the material volume. The adjoint analysis of the integral constraints is the same as that of the design objective. The topology optimization-based computational design problem usually has strong nonlinearity, and it is difficult to solve the system directly. Therefore, the iterative approach is widely adopted. In the iterative approach, the descent direction can be defined based on the adjoint derivative, where the state and adjoint variables are obtained by solving the partial differential equations and corresponding adjoint equations, respectively.

Solving

After adjoint analysis, the computational design problem for SPP nanostructures can be solved using the iterative approach based on the obtained sensitivity information. The procedure for the iterative approach includes the following steps (Table 1): (a) the partial differential equations are solved with the current design variable; (b) the adjoint equations are solved based on the solution of the partial differential equations; (c) the adjoint derivative of the design objective is computed; and (d) the design variable is updated using the method of moving asymptotes (MMA) [55]. The above steps are implemented iteratively until the stopping criteria are satisfied. In this paper, the stopping criterion is specified as the change of the objective values in five consecutive iterations satisfying

$$\tfrac{1}{5} \sum_{i=0}^{4} \left|J_{k-i} - J_{k-i-1}\right| \big/ \left|J_k\right| < \epsilon \tag{14}$$

in the kth iteration, where J_k and γ_k are the objective value and distribution of the design variable in the kth iteration, respectively; ϵ is the tolerance chosen to be 1×10^{-3}. The maximal iterative number is set to be 660. During the solving procedure, the threshold parameter ξ in Eq. 6 is set to be 0.5; the initial value of the projection parameter β is set to be 1 and it is doubled every 60 iterations until the preset maximal value 1024 is reached; the partial differential equations and corresponding adjoint equations are solved by the finite element method using the commercial finite element software $COMSOL\ Multiphysics$ (Version 3.5) [56], where all the numerical implementation are based on the software's basic module: *Comsol Multiphysics* → *PDE Modes* → *PDE, General Form*. For the details on the setting of the *PDE Modes* and numerical integrations, one can refer to [40, 57].

In the computational design of SPP nanostructures, the partial differential equations are solved using the standard Galerkin finite element method. The state variables and corresponding adjoint variables are interpolated quadratically; the Helmholtz filter and corresponding adjoint equations are solved using linear elements; and the design variable is linearly interpolated.

Table 1 Procedure of the iterative solving approach

1. Give the initial values of the design variable
2. Solve the partial differential equations
3. Solve the adjoint equations
4. Compute the adjoint derivative and corresponding objective value
5. Update the design variable using MMA
6. Check for convergence; if the stopping criteria are not satisfied, go to 2
7. Post processing

Results and Discussion

In the following, the computational design problems of SPP nanostructures are, respectively, defined and solved for localized surface plasmon resonances, extraordinary optical transmission, and surface plasmonic cloaking to verify the feasibility and robustness of the proposed topology optimization-based computational design methodology.

Metallic Nanostructures for Localized Surface Plasmon Resonances

Localized surface plasmon resonances (LSPRs) are the strong interaction between metal nanostructures and visible light through the resonant excitations of collective oscillations of conduction electrons. In LSPRs, the local electromagnetic field near the nanostructure can be many orders of magnitude higher than the incident field, and the incident field around the resonant-peak wavelength is scattered strongly; the enhanced electric field is confined within only a tiny region of the nanometer length scale near the surface of the nanostructures and decays significantly thereafter [7]. Surface-enhanced Raman spectroscopy (SERS) is one typical application of LSPRs [11]. In this section, the computational design is carried out for the metallic nanostructures of SERS using the proposed methodology.

In SERS, the strength of LSPRs can be measured by the maximal enhancement factor (EF) defined as $sup_{\mathbf{x}\in\Omega} \frac{|\mathbf{E}|^4}{E_0^4}$, where

$$\mathbf{E} = \frac{1}{j\epsilon_r\epsilon_0\omega}\nabla\times(0, 0, H_z) \tag{15}$$

is the total electric field and $E_0 = \sqrt{\mu_0/\epsilon_0}$ is the amplitude of the electric wave corresponding to the incident magnetic wave. Then, the design objective can be chosen to maximize the enhancement factor

$$J = \frac{1}{f_{e0}}\frac{|\mathbf{E}|^4}{E_0^4}\bigg|_{\mathbf{x}=\mathbf{x}_0} = \frac{1}{f_{e0}}\int_\Omega \frac{|\mathbf{E}|^4}{E_0^4}\delta\left(dist\left(\mathbf{x},\mathbf{x}_0\right)\right)\,\mathrm{d}\Omega \tag{16}$$

where the enhancement factor is normalized by f_{e0}; and f_{e0} is the enhancement factor at $\mathbf{x}_0$, corresponding to the nanostructure with metal material filled the design domain completely; $\mathbf{x}_0$ is the reasonably chosen enhancement position in Ω; $\delta(\cdot)$ is the Dirac function; $dist(\mathbf{x},\mathbf{x}_0)$ is the Euclidian distance between the point $\forall\mathbf{x}\in\Omega$ and the specified position $\mathbf{x}_0$. The enhancement position $\mathbf{x}_0$ should be presented at the surface or coupling position of nanostructures because the maximal enhancement factor must be at the metal surface or coupling position in LSPRs.

For the parameters in the relative permittivity described by the Drude model in Eq. 8, the high-frequency bulk permittivity $\epsilon_{r\infty} = 6$, the bulk plasmon frequency $\omega_p = 1.5\times10^{16}$ rad/s, and the collision frequency $\gamma_c = 7.73\times10^{13}$ rad/s are set by fitting the experimental data in the literature [51]. The computational domain is set to be the square with side length equal to 190 nm; the maximal enhancement position $\mathbf{x}_0$ is chosen to be the center of the square domain Ω (Fig. 1). The incident TM wave, launched from the left boundary, is set as the parallel-plane wave

$$H_{zi} = H_0e^{-jk_0\mathbf{k}\cdot\mathbf{x}} \tag{17}$$

where $H_0 = 1$ is the amplitude of the wave; $\mathbf{k} = \left(k_x, k_y\right)$ is the normalized directional wave vector.

The incident wavelength is scanned in the visible light region (350 ∼ 770 nm). For different incident wavelengths, the obtained topologies of the nanostructures are obtained as shown in Fig. 2a∼h, with corresponding distribution of the magnitude order of enhancement factor $\left(\log\frac{|\mathbf{E}|^4}{E_0^4}\Big|_{\mathbf{x}=\mathbf{x}_0}\right)$ shown in Fig. 3a∼h. The convergent histories of the objective values, corresponding to the computational design of the nanostructure with incident wavelength equal to 770 nm, are shown in Fig. 4, where snapshots for the evolution of the physical density variable are included. In Figs. 2 and 3, the pit configuration is formed at the metal surface to increase the charge density and achieve LSPR at the enhancement position, for short incident wavelengths; the pit configuration is evolved to a tip-slit configuration as the increase of the incident wavelength, where two tips near the enhancement position are presented to increase the charge density, and a slit is formed between these two tips to enforce the given enhancement position to be the coupling position of the two tips and achieve LSPR based on the coupling effect. The enhancement factor spectra of the obtained nanostructures shows that resonant peaks appear at the specified incident wavelengths (Fig. 5). This illustrates the wavelength dependence of the computationally designed LSPR nanostructures; furthermore, it is concluded that the resonant peak of the computationally designed nanostructure can be achieved at a specified incident wavelength, and

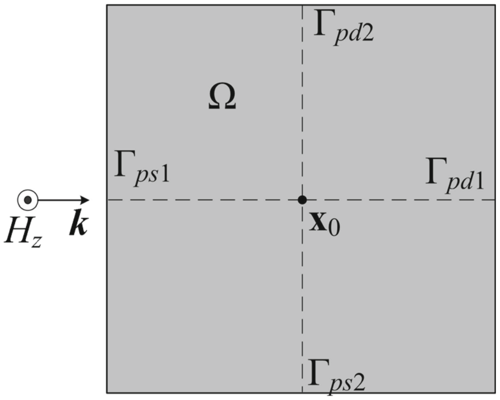

Fig. 1 Schematic for the computational domain of the periodic metallic nanostructures for LSPRs, where Ω is the computational domain, $\mathbf{k}$ is the wave vector, $\mathbf{x}_0$ is the enhancement position specified at the center of the computational domain, and periodic boundary condition of the scattered-field is, respectively, imposed on the two boundary pairs, where the first boundary pair is composed by Γ_{pd1} and Γ_{ps1}, and the second one is composed by Γ_{pd2} and Γ_{ps2}

red or blue shift of the resonant peak can be controlled by specifying larger or smaller wavelength for the corresponding computational design problem.

Periodic Metallic Slits for Extraordinary Optical Transmission

Extraordinary optical transmission (EOT) is the phenomenon of greatly enhanced transmission of light through a subwavelength aperture in an otherwise opaque metallic film which has been patterned with a regularly repeating periodic structure. In EOT, the regularly repeating structure enables much higher transmissivity to occur, up to several orders of magnitude greater than that predicted by classical aperture theory. EOT was first described by Ebbesen et al. [6]. And the mechanism of EOT is attributed to the scattering of SPPs [58, 59]. EOT offers one key advantage over a SPR device, an inherently nano- or microscale device, and it is particularly amenable to miniaturization. To achieve the required transmission performance, metallic layouts with subwavelength apertures, e.g., subwavelength hole array [6], periodic slit array, tapered slits [60], diatomic chain of slit-hole [61], groove array flanking slit [62], and bull's eye structures [63], have been proposed for EOT, and parametric optimization of metallic layouts with subwavelength apertures have been implemented to enhance the transmissivity [64, 65]. This section is devoted to addressing the more challenging problem on full-parameter computational design of the periodic metallic slits for EOT to enhance the transmissivity.

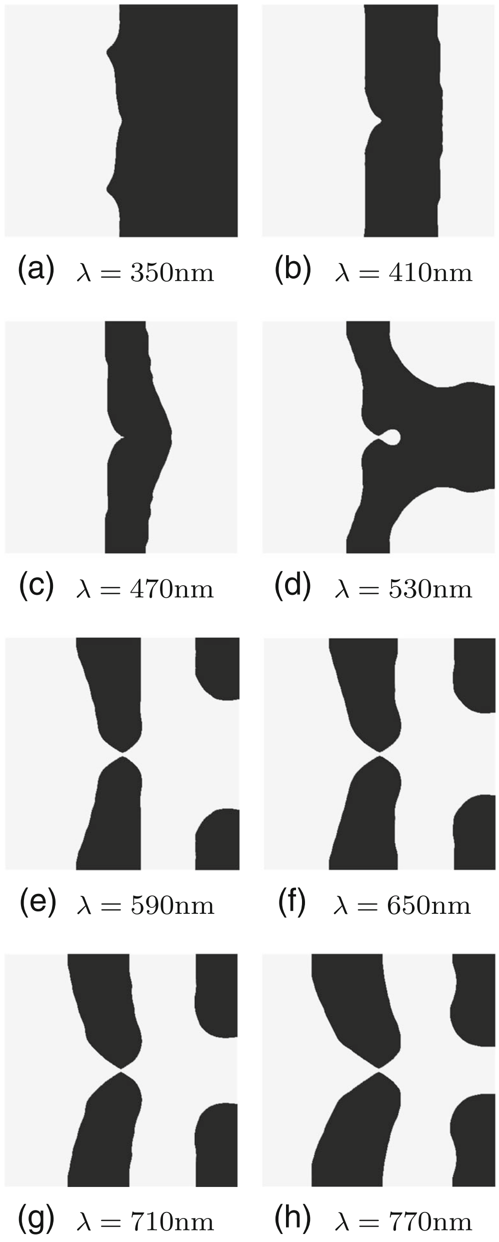
(a) $\lambda = 350\mathrm{nm}$ (b) $\lambda = 410\mathrm{nm}$
(c) $\lambda = 470\mathrm{nm}$ (d) $\lambda = 530\mathrm{nm}$
(e) $\lambda = 590\mathrm{nm}$ (f) $\lambda = 650\mathrm{nm}$
(g) $\lambda = 710\mathrm{nm}$ (h) $\lambda = 770\mathrm{nm}$

Fig. 2 Computationally, designed topologies of the SERS silver cells corresponding to different incident wavelengths in the visible light region, where the enhancement factor is maximized at the center of the computational domain shown in Fig. 1

In periodic metallic slits, EOT is featured by its high transmission of the optical energy. The input and output transmission power for one period of the metallic slits demonstrated in Fig. 6 can be measured by the integration of the average Poynting vector

$$\begin{aligned} P_i &= \int_{\Gamma_{ab1}} -\frac{1}{2}\mathrm{Re}\left(\mathbf{E}_i \times \mathbf{H}_i^*\right)\cdot\mathbf{n}\,\mathrm{d}\Gamma \\ &= \int_{\Gamma_{ab1}} \frac{1}{2}\sqrt{\frac{\mu_0\mu_r}{\epsilon_0\epsilon_r}} H_{zi} H_{zi}^*\,\mathrm{d}\Gamma \\ P_o &= \int_{\Gamma_{ab2}} \frac{1}{2}\mathrm{Re}\left(\mathbf{E} \times \mathbf{H}^*\right)\cdot\mathbf{n}\,\mathrm{d}\Gamma \\ &= \int_{\Gamma_{ab2}} \frac{1}{2}\sqrt{\frac{\mu_0\mu_r}{\epsilon_0\epsilon_r}} H_z H_z^*\,\mathrm{d}\Gamma \end{aligned} \quad (18)$$

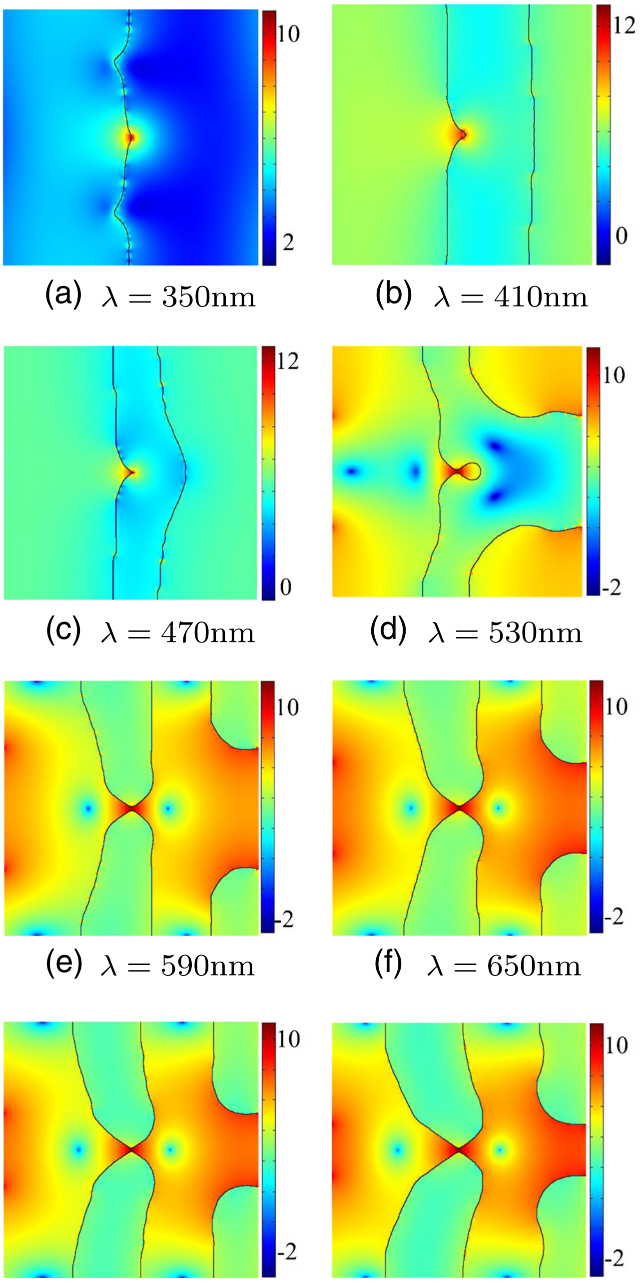

(a) $\lambda = 350\text{nm}$ (b) $\lambda = 410\text{nm}$

(c) $\lambda = 470\text{nm}$ (d) $\lambda = 530\text{nm}$

(e) $\lambda = 590\text{nm}$ (f) $\lambda = 650\text{nm}$

(g) $\lambda = 710\text{nm}$ (h) $\lambda = 770\text{nm}$

Fig. 3 Distribution of the magnitude order of the enhancement factor corresponding to the computationally designed cells in Fig. 2a∼h, respectively

where $*$ represents the conjugate of the complex quantity; P_i and P_o are the input and output transmission power, respectively; Γ_{ab1} and Γ_{ab2}, set to be first-order absorbing type, are respectively the input and output boundary of the TM wave as shown in Fig. 6; $\mathbf{E}_i$ is the electric field corresponding to the incident magnetic wave $\mathbf{H}_i = (0, 0, H_{zi})$; $\mathbf{E}$ is the total electric field; $\mathbf{H}$ is the total magnetic field. $\mathbf{E}_i$ and $\mathbf{E}$ in Eq. 18 can be derived using Eq. 15. Then, the design objective of the metallic slit can be chosen to maximize the transmissivity defined as the normalized transmission power

$$J = P_o / P_i \tag{19}$$

With the incident wave set to be the same as that in "Metallic Nanostructures for Localized Surface Plasmon Resonances" section, the input power P_i is constant. Therefore, the sensitivity analysis is only necessary to implemented for the transmission power P_o using the procedure introduced in "Analyzing" section.

The periodic metallic slits with silver material are investigated in free space for EOT, where the parameters of the Drude model for relative permittivity are the same as that in "Metallic Nanostructures for Localized Surface Plasmon Resonances" section. The sizes of the computational domain shown in Fig. 6 are set to be the typical values: 1050 nm for the periodic length of the metallic slit, 40 nm for the slit width, 350 nm for the thickness of the fixed silver layers, and 350 nm for the thickness of the design domain. The incident wave with the form of parallel-plan wave in Eq. 17 is launched from the left boundary in the positive direction of the x-axis.

In the visible light region, the metallic slit formed by the fixed silver layers shown in Fig. 6 has two transmission peaks corresponding to the incident wavelength 526 and 616 nm, respectively. Then, by choosing the incident wavelength to respectively be 526 and 616 nm, the nanoscale structural topologies of the metallic slits are obtained as shown in Fig. 7 with corresponding distribution of the magnetic fields shown in Fig. 8. The convergent histories of the objective values, corresponding to the computational design of the metallic slit with incident wavelength equal to 526 nm, are shown in Fig. 9, including snapshots for the evolution of the physical density variable. Based on the computational design method, the transmissivity of the obtained metallic slits is enhanced 3.27 and 4.06 times compared with that of the slits formed by the fixed silver layers in Fig. 6, respectively, and transmission peaks in the spectra of the designed metallic slits are achieved at the corresponding incident wavelengths (Fig. 10). This demonstrates the effectivity of the outlined computational design method on the enhancement of EOT performance of nanostructures. The magnetic field in Fig. 8 demonstrate that the metallic configuration formed at the inlet side of the computationally designed slit excites SPP and guides it to propagate along the two sides of the slit; the propagating SPP at the two sides of the metallic slit is coupled and resonated, where Fabry-Pérot resonance behavior is established and the transmission is strengthened [66–70]; the resonated SPP is guided and radiated into free space by the metallic configuration formed at the outlet side of the slit, and EOT is achieved and strengthened based on the computational design method.

Fig. 4 Convergent histories of the objective values and snapshots for the evolution of the physical density variable, corresponding to the computational design of the LSPR nanostructure with incident wavelength equal to 770 nm

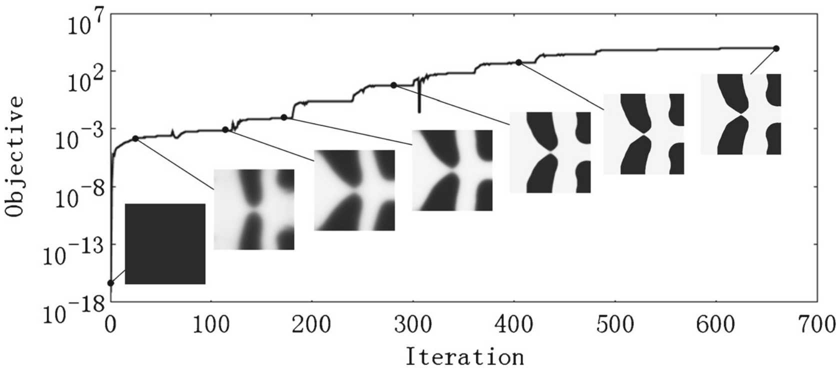

Fig. 5 Enhancement factor spectra of the computationally designed nanostructures (Fig. 2a∼h) at the specified enhancement position

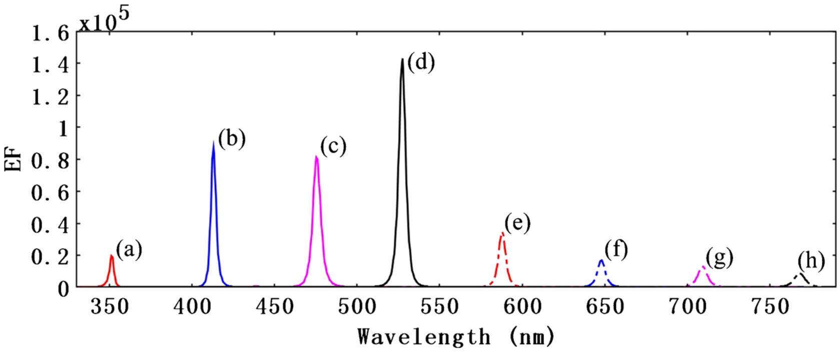

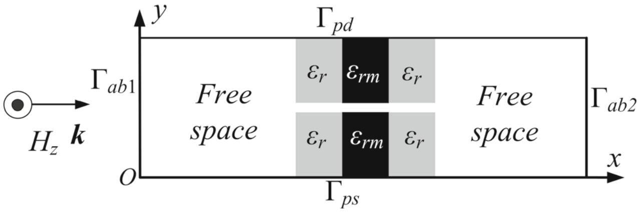

Fig. 6 Schematic for the computational domain of the periodic metallic slits, where H_z is the propagating TM wave; $\mathbf{k}$ is the normalized wave vector; Γ_{ab1} and Γ_{ab2}, respectively, are the input and output boundary of the metallic slit; Γ_{ps} and Γ_{pd} are the source and destination boundary of the periodic boundary pair. In the computational domain, there is a fixed metallic slit with relative permittivity ϵ_{rm}; two pieces of design domain with interpolated relative permittivity ϵ_r are located at the bilateral of the fixed metallic slit; and the other area of the computational domain is free space

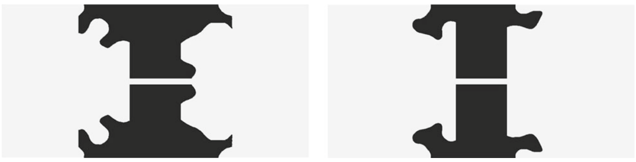

(a) $\lambda = 526\text{nm}$ (b) $\lambda = 616\text{nm}$

Fig. 7 Computationally designed metallic slits for extraordinary optical transmission corresponding to different incident wavelengths in the visible light region

From the transmission spectra shown in Fig. 10, one can see that there are second peaks for the computationally designed metallic slits with incident wavelengths at 575 and 725 nm, respectively. The magnetic field distribution corresponding to the second peaks of the transmission spectra is shown in Fig. 11, where SPP is also excited effectively at the inlet side of the computationally designed metallic slits, and the propagating SPP is guided into the metallic slits. Increase of the incident wavelength is helpful for the coupling and resonance of the SPP propagating along the two sides of the metallic slits. Therefore, the second peaks are presented as shown in Fig. 10. However, the metallic slits can be redesigned using the proposed method by setting the incident wavelengths, respectively, at 575 and 725 nm to derived more efficient EOT. Then the computationally designed metallic slits in Fig. 12 are obtained with transmissivity spectra shown in Fig. 13.

To demonstrate the effect of the slit thickness, several metallic slits are computationally designed using the proposed method by choosing different slit thicknesses. The obtained computational designs and corresponding transmissivity with incident wavelength 526 nm are plotted in Fig. 14. From these results, one can see that reasonably reducing the slit thickness can enhance the transmissivity, where the Fabry-Pérot resonance behavior is achieved and SPP propagation distance and energy absorption are reduced.

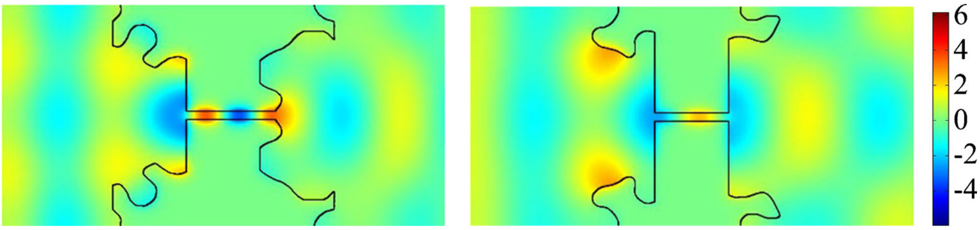

(a) $\lambda = 526\text{nm}$ (b) $\lambda = 616\text{nm}$

Fig. 8 Magnetic field distribution in the computationally designed metallic slits, respectively, corresponding to the topological configurations shown in Fig. 7a, b

Surface Plasmonic Cloaking

The technique of transformation optics (TO) provides a powerful means to precisely control bulk optical waves in almost arbitrary ways [71, 72]. With TO technique, the optical cloak has been designed to hide a given object for a specific frequency range in the electromagnetic spectrum [71, 72]. The TO designed cloak usually has extreme electromagnetic properties. And they are achieved based on the use of metamaterials. The tailored microstructure of such metamaterials has to be much smaller than the wavelength, and this makes it very challenging to realize the desired magnetic properties for optical frequencies. To solve this problem, the topology optimization-based computational design method has been utilized to design cloak using conventional simple isotropic dielectric media readily available in nature [22–24]. Correspondingly, the technique of transformational plasmon optics (TPO) has also been developed for precisely controlling SPPs [8, 9]. With TPO technique, SPPs can be tightly bounded at curved metal-dielectric interfaces to reduce the scattering losses and achieve SP cloaking, where the propagation of SPPs can be manipulated in a prescribed manner by carefully controlling the properties of the material adjoined to a metal. However, the extreme electromagnetic properties of the TPO design still needs to be achieved based on the use of metamaterials. Therefore, this section will use the topology optimization-based computational design method to solve this problem based on the conventional isotropic dielectrics.

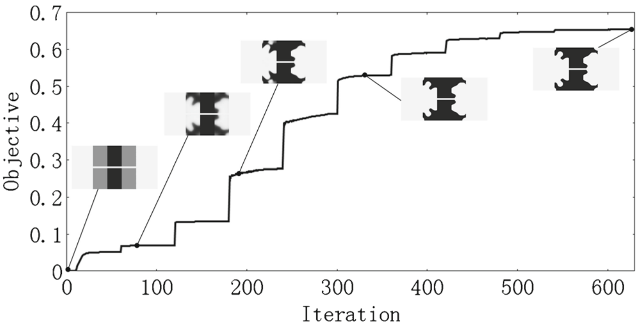

Fig. 9 Convergent histories of the objective values and snapshots for the evolution of the physical density variable, corresponding to the computationally designed metallic silt for extraordinary optical transmission with incident wavelength equal to 526 nm

SPP propagation can be scattered by the curved metal-free space interface and radiated into the free space. To achieve the cloaking of the curved part of interface to SPP propagation, the topology optimization-based computational design method can be used to implement the design of the dielectric cloak covered on the curved part of the interface. Then the design objective can be chosen to minimize the norm of the scattered field

$$J = \frac{1}{J_0} \int_{\Omega_f} H_{zs} H_{zs}^* \, \mathrm{d}\Omega \tag{20}$$

where the objective is normalized by J_0 corresponding to the norm of the scattered field without dielectric cloak covered on the curved interface. The computational domain, with all the boundaries set to be first-order absorbing type, is shown in Fig. 15a, where Ω_f is the free space with relative permittivity $\epsilon_{rf} = 1$, Ω_d is the design domain of the SP cloak, and Ω_m is the metallic domain filled with silver

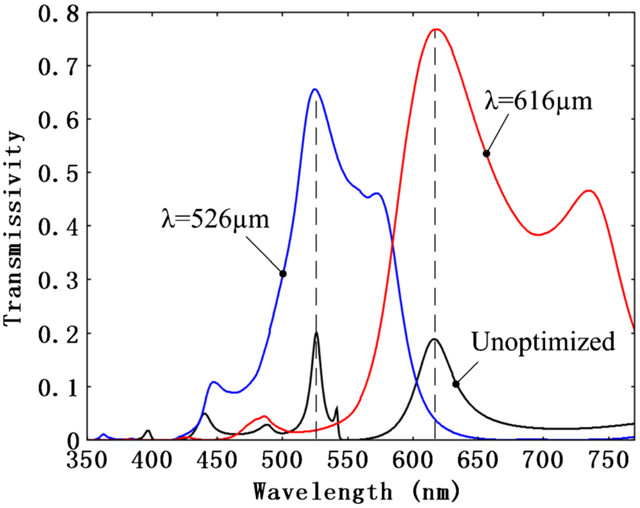

Fig. 10 Transmission spectra of the computationally designed metallic slits shown in Fig. 7 and the metallic slit formed by the fixed silver layers in Fig. 6. There are two transmission peaks at the wavelength 526 and 616 nm of the fixed metallic slit. Based on the topology optimization-based computational design method, these two transmission peaks are enhanced 3.27 and 4.06 times, respectively

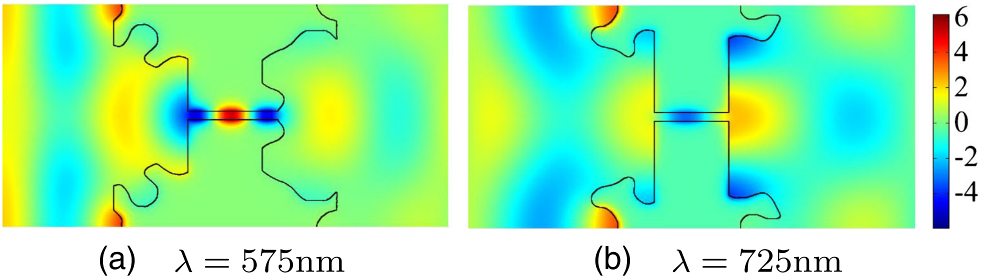

(a) $\lambda = 575\text{nm}$ (b) $\lambda = 725\text{nm}$

Fig. 11 Magnetic field distribution corresponding to the second peaks of the transmission spectra of the computationally designed metallic slits shown in Fig. 7

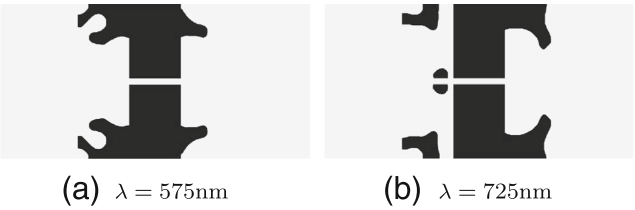

(a) $\lambda = 575\text{nm}$ (b) $\lambda = 725\text{nm}$

Fig. 12 Computationally designed metallic slits for extraordinary optical transmission corresponding to the incident wavelengths 575 and 725 nm

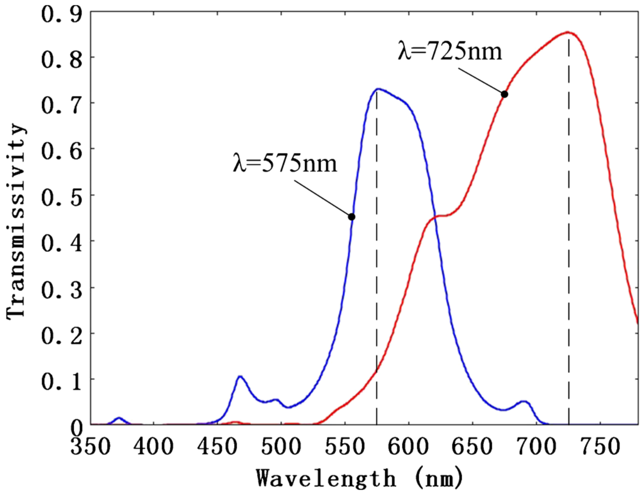

Fig. 13 Transmission spectra of the computationally designed metallic slits shown in Fig. 12

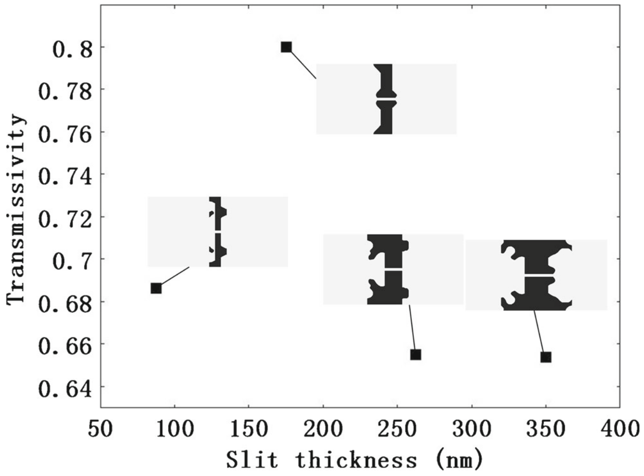

Fig. 14 Computationally designed metallic slits with different thicknesses and the corresponding transmissivity

material with the same choice of Drude model parameters as that in "Metallic Nanostructures for Localized Surface Plasmon Resonances" section. The incident wave is set to be the SPP propagating at the flat interface without curved part (Fig. 15b)

$$H_{zi} = \begin{cases} H_0 e^{-j\beta_{SPP}x - k_{fy}y}, & y \ge 0 \\ H_0 e^{-j\beta_{SPP}x + k_{my}y}, & y < 0 \end{cases} \tag{21}$$

where $H_0 = 1$ is the amplitude of the incident wave; $\beta_{SPP} = k_0\sqrt{\frac{\epsilon_{rf}\epsilon_{rm}}{\epsilon_{rf}+\epsilon_{rm}}}$ is the propagation constant of SPP; $k_{fy} = \sqrt{\beta_{SPP}^2 - k_0^2\epsilon_{rf}}$ and $k_{my} = \sqrt{\beta_{SPP}^2 - k_0^2\epsilon_{rm}}$ are the wave numbers of SPP in free space and metal, respectively. The SPP propagation scattered by the curved interface expressed as

$$y = \begin{cases} \lambda\cos^2\left(\frac{x-12\lambda}{6\lambda}\pi\right), & 9\lambda \le x \le 15\lambda \\ 0, & x < 9\lambda \text{ or } x > 15\lambda \end{cases} \tag{22}$$

is shown in Fig. 15c, where the SPP is broken away from the interface and radiated into the free space.

Based on the above presetting, the SP cloak shown in Fig. 15d is obtained using the proposed methodology with material interpolation between dielectric and free space, where the isotropic dielectric with relative permittivity equal to 2 is utilized. The corresponding SPP distribution at the cloaked interface is shown in Fig. 15e. The convergent histories of the objective values are shown in Fig. 15f, with snapshots for the evolution of the physical density variable. Using the designed cloak covered at the curved part of the interface, the energy of the scattering field is reduced to be 5.06 % of that of the uncloaked case with field distribution shown in Fig. 15c, and the SPP propagation is bounded at the interface and radiation of the field is removed as shown in Fig. 15e, which demonstrates that phase match is achieved for the SPP propagation behind the curved part of the interface. Therefore, cloaking of the curved part of

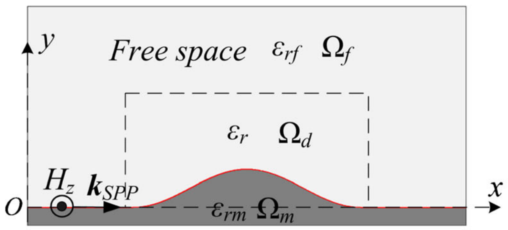

(a) Computational domain of the SP cloak

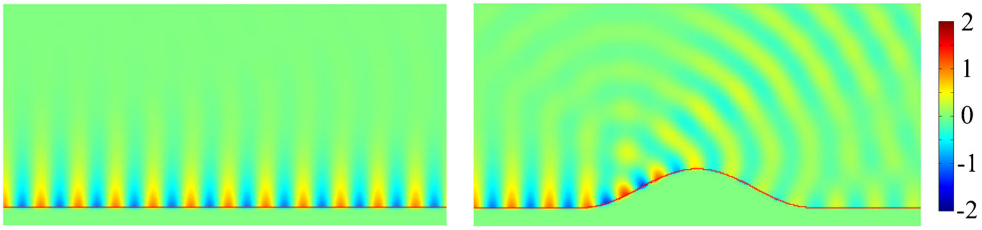

(b) Incident SPP H_{zi} (c) Scattered SPP

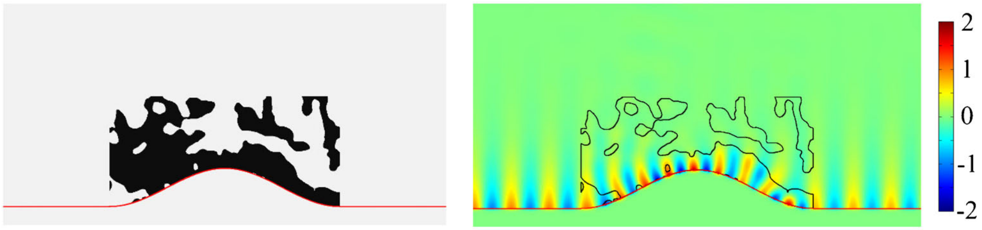

(d) SP cloak topology (e) Cloaked SPP

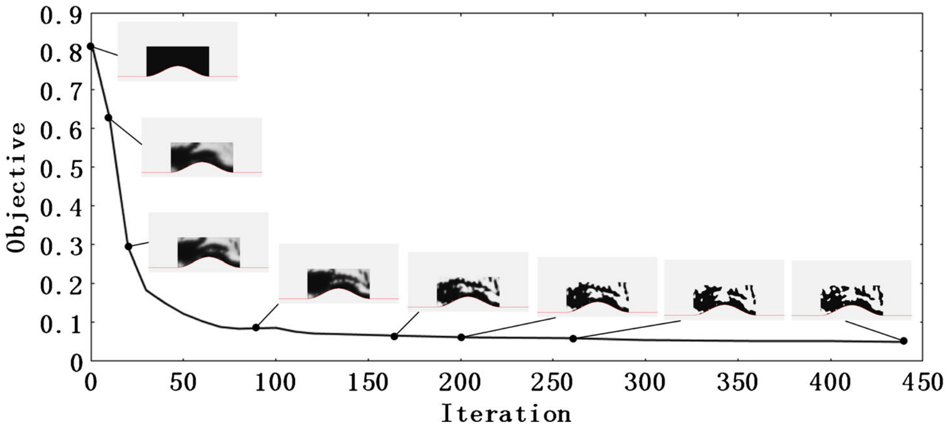

(f) Convergent history

Fig. 15 **a** Computational domain of the SP cloak, where Ω_f is the free space with relative permittivity $\epsilon_{rf} = 1$, Ω_m is the metallic domain with relative permittivity ϵ_{rm}, and Ω_d is the design domain with relative permittivity ϵ_r interpolated between free space and the dielectric with relative permittivity equal to 2; **b** field distribution of the incident SPP wave H_{zi} analytically expressed in Eq. 21; **c** field distribution of the scattered SPP wave at the curved interface expressed in Eq. 22; **d** SP cloak designed using the computational design method; **e** field distribution of the SPP wave at the curved interface covered by the designed cloak; **f** convergent histories of the objective values, with snapshots for the evolution of the physical density variable

the interface is realized for the SPP propagation, with the cloak computationally designed using conventional simple isotropic dielectric, which is readily available in nature.

Conclusion

This paper has developed and implemented a topology optimization-based computational design method for nanostructures in surface plasmon polaritons. This method allows user to design nanostructures solely based on the desired performance of surface plasmon polaritons, where the minimum length scale of the derived nanostructures can be ensured by the filter and projection techniques. The capability and robustness of the proposed method has been demonstrated by designing various nanostructures for localized plasmonic resonances, extraordinary optical transmission, and surface plasmonic cloaking.

In addition, the computational design method can also be extended to implement the inverse design of other nanostructures for surface plasmon polaritons, e.g., optical trapping and optical antenna. This will also be helpful for the designer to give more reasonable nano-optics design to cater for the engineering requirement.

Acknowledgments The authors are grateful to Professor K. Svanberg for supplying the MMA codes. This work is supported by the National Natural Science Foundation of China (Nos. 51405465, 51275504, 51205381).

Appendix

The details on deriving the adjoint equations and derivative of the computational design problem in Eq. 9 are presented as follows. According to the Lagrangian multiplier method, the augmented Lagrangian functional corresponding to the variational problem in Eq. 9 can be introduced as

$$\begin{aligned}\hat{J} = &\int_\Omega A\left(H_{zs}, \nabla H_{zs}, \rho_{fp}; \rho\right) \mathrm{d}\Omega + \int_{\partial\Omega} B\left(H_{zs}\right) \mathrm{d}\Gamma \\ &+\Phi\left(H_{zs}, \nabla H_{zs}, \rho_{fp}; \rho\right) + \Psi\left(\rho_f, \nabla\rho_f; \rho\right)\end{aligned} \tag{23}$$

where

$$\begin{aligned}\Phi\left(H_{zs}, \nabla H_{zs}, \rho_{fp}; \rho\right) = &\int_\Omega -\epsilon_r^{-1}\nabla\left(H_{zs}+H_{zi}\right)\cdot\nabla\tilde{H}_{zs}^* \\ &+k_0^2\mu_r\left(H_{zs}+H_{zi}\right)\tilde{H}_{zs}^* + \int_{\Gamma_{ab}}\Big(-jk_0\sqrt{\epsilon_r^{-1}\mu_r}H_{zs} \\ &+\epsilon_r^{-1}\nabla H_{zi}\cdot\mathbf{n}\Big)\tilde{H}_{zs}^*\,\mathrm{d}\Gamma + \int_{\Gamma_{pd}}\epsilon_r^{-1}\nabla\left(H_{zs}+H_{zi}\right)\cdot \\ &\mathbf{n}\tilde{H}_{zs}^*\,\mathrm{d}\Gamma + \int_{\Gamma_{ps}}\epsilon_r^{-1}\nabla\left(H_{zs}+H_{zi}\right)\cdot\mathbf{n}\tilde{H}_{zs}^*\,\mathrm{d}\Gamma \\ &+\int_{\Gamma_{sm}}\epsilon_r^{-1}\nabla H_{zi}\cdot\mathbf{n}\tilde{H}_{zs}^*\,\mathrm{d}\Gamma\end{aligned} \tag{24}$$

$$\begin{aligned}\Psi\left(\rho_f, \nabla\rho_f; \rho\right) = &\int_\Omega r^2\nabla\rho_f\cdot\nabla\tilde{\rho}_f^*\,\mathrm{d}\Omega \\ &+\int_\Omega \rho_f\tilde{\rho}_f^*\,\mathrm{d}\Omega - \int_\Omega \rho\tilde{\rho}_f^*\,\mathrm{d}\Omega\end{aligned} \tag{25}$$

$\tilde{H}_{zs}$ and $\tilde{\rho}_f$ are the adjoint variables of H_{zs} and ρ_f, respectively; $\tilde{H}_{zs}$ satisfies the same periodicity as H_{zs}. H_{zs} and ρ_f are distributions in $\mathcal{H}^1(\Omega)$, the first-order Sobolev space defined on Ω; $\tilde{H}_{zs}$ and $\tilde{\rho}_f$ are distributions in $\mathcal{H}^{1*}(\Omega)$, the dual space of $\mathcal{H}^1(\Omega)$; ρ is the distribution in $\mathcal{L}^2(\Omega)$, the second-order Lebesgue integrable functional space; for functional space, $*$ represents the dual space; for complex, $*$ represents the conjugate operation. Because of the periodicity of the field expressed by the periodic boundary condition, it is satisfied that

$$\begin{aligned}&\int_{\Gamma_{pd}}\epsilon_r^{-1}\nabla\left(H_{zs}+H_{zi}\right)\cdot\mathbf{n}\tilde{H}_{zs}^*\,\mathrm{d}\Gamma \\ &\quad+\int_{\Gamma_{ps}}\epsilon_r^{-1}\nabla\left(H_{zs}+H_{zi}\right)\cdot\mathbf{n}\tilde{H}_{zs}^*\,\mathrm{d}\Gamma = 0\end{aligned} \tag{26}$$

Then Eq. 24 can be reduced to be

$$\begin{aligned}\Phi\left(H_{zs}, \nabla H_{zs}, \rho_{fp}; \rho\right) = &\int_\Omega -\epsilon_r^{-1}\nabla\left(H_{zs}+H_{zi}\right)\cdot\nabla\tilde{H}_{zs}^* \\ &+k_0^2\mu_r\left(H_{zs}+H_{zi}\right)\tilde{H}_{zs}^*\,\mathrm{d}\Omega \\ &+\int_{\Gamma_{ab}}\left(-jk_0\sqrt{\epsilon_r^{-1}\mu_r}H_{zs}+\epsilon_r^{-1}\nabla H_{zi}\cdot\mathbf{n}\right)\tilde{H}_{zs}^*\,\mathrm{d}\Gamma \\ &+\int_{\Gamma_{pd}\bigcup\Gamma_{ps}\bigcup\Gamma_{sm}}\epsilon_r^{-1}\nabla H_{zi}\cdot\mathbf{n}\tilde{H}_{zs}^*\,\mathrm{d}\Gamma\end{aligned} \tag{27}$$

From the first-order variational of $\hat{J}$, one can obtain

$$\begin{aligned}\left\langle\frac{\delta\hat{J}}{\delta\rho}, \delta\rho\right\rangle_{\mathcal{L}^{2*},\mathcal{L}^2} = &\left\langle J_{H_{zs}}, \delta H_{zs}\right\rangle_{\mathcal{H}^{1*},\mathcal{H}^1} + \left\langle\Phi_{H_{zs}}, \delta H_{zs}\right\rangle_{\mathcal{H}^{1*},\mathcal{H}^1} \\ &+\left\langle J_{\nabla H_{zs}}, \nabla\delta H_{zs}\right\rangle_{\boldsymbol{\mathcal{L}}^{2*},\boldsymbol{\mathcal{L}}^2} + \left\langle\Phi_{\nabla H_{zs}}, \nabla\delta H_{zs}\right\rangle_{\boldsymbol{\mathcal{L}}^{2*},\boldsymbol{\mathcal{L}}^2} \\ &+\left\langle J_{\rho_{fp}}\rho_{fp_{\rho_f}}, \delta\rho_f\right\rangle_{\mathcal{H}^{1*},\mathcal{H}^1} + \left\langle\Phi_{\rho_{fp}}\rho_{fp_{\rho_f}}, \delta\rho_f\right\rangle_{\mathcal{H}^{1*},\mathcal{H}^1} \\ &+\left\langle\Psi_{\rho_f}, \delta\rho_f\right\rangle_{\mathcal{H}^{1*},\mathcal{H}^1} + \left\langle\Psi_{\nabla\rho_f}, \nabla\delta\rho_f\right\rangle_{\boldsymbol{\mathcal{L}}^{2*},\boldsymbol{\mathcal{L}}^2} \\ &+\left\langle J_\rho, \delta\rho\right\rangle_{\mathcal{L}^{2*},\mathcal{L}^2} + \left\langle\Psi_\rho, \delta\rho\right\rangle_{\mathcal{L}^{2*},\mathcal{L}^2}\end{aligned} \tag{28}$$

where $\langle\cdot,\cdot\rangle$ represents the dual pairing between two dual spaces; $\delta H_{zs} \in \mathcal{H}^1(\Omega)$, $\delta\rho_f \in \mathcal{H}^1(\Omega)$ and $\delta\rho \in \mathcal{L}^2(\Omega)$ are, respectively, the first-order variational of H_{zs}, ρ_f, and ρ; $\boldsymbol{\mathcal{L}}^2(\Omega)$ is the vector valued second-order Lebesgue integrable functional space. According to the Kurash-Kuhn-Tucker condition [52] and setting

$$\begin{aligned}&\left\langle J_{H_{zs}}, \delta H_{zs}\right\rangle_{\mathcal{H}^{1*},\mathcal{H}^1} + \left\langle\Phi_{H_{zs}}, \delta H_{zs}\right\rangle_{\mathcal{H}^{1*},\mathcal{H}^1} \\ &\quad+\left\langle J_{\nabla H_{zs}}, \nabla\delta H_{zs}\right\rangle_{\boldsymbol{\mathcal{L}}^{2*},\boldsymbol{\mathcal{L}}^2} + \left\langle\Phi_{\nabla H_{zs}}, \nabla\delta H_{zs}\right\rangle_{\boldsymbol{\mathcal{L}}^{2*},\boldsymbol{\mathcal{L}}^2} = 0 \\ &\left\langle J_{\rho_{fp}}\rho_{fp_{\rho_f}}, \delta\rho_f\right\rangle_{\mathcal{H}^{1*},\mathcal{H}^1} + \left\langle\Phi_{\rho_{fp}}\rho_{fp_{\rho_f}}, \delta\rho_f\right\rangle_{\mathcal{H}^{1*},\mathcal{H}^1} \\ &\quad+\left\langle\Psi_{\rho_f}, \delta\rho_f\right\rangle_{\mathcal{H}^{1*},\mathcal{H}^1} + \left\langle\Psi_{\nabla\rho_f}, \nabla\delta\rho_f\right\rangle_{\boldsymbol{\mathcal{L}}^{2*},\boldsymbol{\mathcal{L}}^2} = 0\end{aligned} \tag{29}$$

the adjoint equations of Eqs. 1 and 6 in weak forms can be obtained as follows:

$$\begin{aligned}
&\int_{\Omega} -\epsilon_r^{-1} \nabla \delta H_{zs} \cdot \nabla \tilde{H}_{zs}^{*} \\
&\quad + \left(k_0^2 \mu_r \tilde{H}_{zs}^{*} + \frac{\partial A}{\partial H_{zs}} - \nabla \cdot \frac{\partial A}{\partial \nabla H_{zs}} \right) \delta H_{zs} \, \mathrm{d}\Omega \\
&\quad + \int_{\Gamma_{ab}} \left(-jk_0 \sqrt{\epsilon_r^{-1} \mu_r} \tilde{H}_{zs}^{*} + \frac{\partial A}{\partial \nabla H_{zs}} \cdot \mathbf{n} + \frac{\partial B}{\partial H_{zs}} \right) \delta H_{zs} \, \mathrm{d}\Gamma \\
&\quad + \int_{\Gamma_{pd} \bigcup \Gamma_{ps} \bigcup \Gamma_{sm}} \left(\frac{\partial A}{\partial \nabla H_{zs}} \cdot \mathbf{n} + \frac{\partial B}{\partial H_{zs}} \right) \delta H_{zs} \, \mathrm{d}\Gamma = 0 \\
&\quad \Longleftrightarrow \\
&\int_{\Omega} -\epsilon_r^{-1} \nabla \tilde{H}_{zs}^{*} \cdot \nabla \hat{\tilde{H}}_{zs} \\
&\quad + \left(k_0^2 \mu_r \tilde{H}_{zs}^{*} + \frac{\partial A}{\partial H_{zs}} - \nabla \cdot \frac{\partial A}{\partial \nabla H_{zs}} \right) \hat{\tilde{H}}_{zs} \, \mathrm{d}\Omega \\
&\quad + \int_{\Gamma_{ab}} \left(-jk_0 \sqrt{\epsilon_r^{-1} \mu_r} \tilde{H}_{zs}^{*} + \frac{\partial A}{\partial \nabla H_{zs}} \cdot \mathbf{n} + \frac{\partial B}{\partial H_{zs}} \right) \hat{\tilde{H}}_{zs} \, \mathrm{d}\Gamma \\
&\quad + \int_{\Gamma_{pd} \bigcup \Gamma_{ps} \bigcup \Gamma_{sm}} \left(\frac{\partial A}{\partial \nabla H_{zs}} \cdot \mathbf{n} + \frac{\partial B}{\partial H_{zs}} \right) \hat{\tilde{H}}_{zs} \, \mathrm{d}\Gamma = 0, \\
&\quad \text{for } \forall \hat{\tilde{H}}_{zs} \in \mathcal{H}^1 (\Omega)
\end{aligned} \tag{30}$$

and

$$\begin{aligned}
&\int_{\Omega} r^2 \nabla \delta\rho_f \cdot \nabla \tilde{\rho}_f^{*} \\
&+ \left[\tilde{\rho}_f^{*} + \frac{\partial A}{\partial \rho_{fp}} \frac{\partial \rho_{fp}}{\partial \rho_f} - \frac{\partial \epsilon_r^{-1}}{\partial \rho_{fp}} \frac{\partial \rho_{fp}}{\partial \rho_f} \nabla \left(H_{zs} + H_{zi} \right) \cdot \nabla \tilde{H}_{zs}^{*} \right] \delta\rho_f \, \mathrm{d}\Omega \\
&+ \int_{\Gamma_{ab}} \left(-jk_0 \frac{\partial \sqrt{\epsilon_r^{-1}}}{\partial \rho_{fp}} \sqrt{\mu_r} H_{zs} + \frac{\partial \epsilon_r^{-1}}{\partial \rho_{fp}} \nabla H_{zi} \cdot \mathbf{n} \right) \tilde{H}_{zs}^{*} \frac{\partial \rho_{fp}}{\partial \rho_f} \delta\rho_f \, \mathrm{d}\Gamma \\
&+ \int_{\Gamma_{pd} \bigcup \Gamma_{ps} \bigcup \Gamma_{sm}} \frac{\partial \epsilon_r^{-1}}{\partial \rho_{fp}} \frac{\partial \rho_{fp}}{\partial \rho_f} \nabla H_{zi} \cdot \mathbf{n} \tilde{H}_{zs}^{*} \delta\rho_f \, \mathrm{d}\Gamma = 0 \\
&\quad \Longleftrightarrow \\
&\quad \int_{\Omega} r^2 \nabla \tilde{\rho}_f^{*} \cdot \nabla \hat{\tilde{\rho}}_f \\
&+ \left[\tilde{\rho}_f^{*} + \frac{\partial A}{\partial \rho_{fp}} \frac{\partial \rho_{fp}}{\partial \rho_f} - \frac{\partial \epsilon_r^{-1}}{\partial \rho_{fp}} \frac{\partial \rho_{fp}}{\partial \rho_f} \nabla \left(H_{zs} + H_{zi} \right) \cdot \nabla \tilde{H}_{zs}^{*} \right] \hat{\tilde{\rho}}_f \, \mathrm{d}\Omega \\
&+ \int_{\Gamma_{ab}} \left(-jk_0 \frac{\partial \sqrt{\epsilon_r^{-1}}}{\partial \rho_{fp}} \sqrt{\mu_r} H_{zs} + \frac{\partial \epsilon_r^{-1}}{\partial \rho_{fp}} \nabla H_{zi} \cdot \mathbf{n} \right) \tilde{H}_{zs}^{*} \frac{\partial \rho_{fp}}{\partial \rho_f} \hat{\tilde{\rho}}_f \, \mathrm{d}\Gamma \\
&+ \int_{\Gamma_{pd} \bigcup \Gamma_{ps} \bigcup \Gamma_{sm}} \frac{\partial \epsilon_r^{-1}}{\partial \rho_{fp}} \frac{\partial \rho_{fp}}{\partial \rho_f} \nabla H_{zi} \cdot \mathbf{n} \tilde{H}_{zs}^{*} \hat{\tilde{\rho}}_f \, \mathrm{d}\Gamma = 0, \\
&\text{for } \forall \hat{\tilde{\rho}}_f \in \mathcal{H}^1 (\Omega)
\end{aligned} \tag{31}$$

Based on the arbitrariness of $\hat{\tilde{H}}_{zs}$ and $\hat{\tilde{\rho}}_f$ and Gauss theory [52], the weak forms in Eqs. 30 and 31 can be transformed into the strong forms of the adjoint Eqs. 11 and 12. After the derivation of the adjoint equations, the adjoint derivative of the computational design problem can be further obtained as

$$\begin{aligned}
&\left\langle \tfrac{\delta \hat{J}}{\delta \rho}, \delta\rho \right\rangle_{\mathcal{L}^{2*}, \mathcal{L}^2} \\
&= \left\langle J_\rho, \delta\rho \right\rangle_{\mathcal{L}^{2*}, \mathcal{L}^2} + \left\langle \Psi_\rho, \delta\rho \right\rangle_{\mathcal{L}^{2*}, \mathcal{L}^2} \\
&= \int_\Omega \left(\tfrac{\partial A}{\partial \rho} - \tilde{\rho}_f^{*} \right) \delta\rho \, \mathrm{d}\Omega
\end{aligned} \tag{32}$$

which can be transformed into the strong form

$$\tfrac{\delta \hat{J}}{\delta \rho} = \tfrac{\partial A}{\partial \rho} - \tilde{\rho}_f^{*}, \text{ in } \Omega \tag{33}$$

In the adjoint derivative, only the real part is utilized because the design variable ρ is the distribution defined on real space.

References

1. Economou EN (1969) Surface plasmons in thin films. Phys Rev 182:2
2. Raether H (1988) Surface plasmons on smooth and rough surfaces and on gratings. Springer
3. Maier SA (2007) Plasmonics: fundamentals and applications. Springer Science + Business Media LCC, New York
4. Zayats AV, Smolyaninov II, Maradudin AA (2004) Nano-optics of surface plasmon polaritons. Phys Reports 408:131–313
5. Zia R, Selker MD, Brongersma ML (2005) Leaky and bound modes of surface plasmon waveguides. Phys Rev B 71:165–431
6. Ebbesen TW, Lezec HJ, Ghaemi HF, Thio T, Wolff PA (1998) Extraordinary optical transmission through sub-wavelength hole arrays. Nature 391:667–669
7. Su KH, Wei QH, Zhang X, Mock JJ, Smith DR, Schultz S (2003) Interparticle coupling effects on plasmon resonances of nanogold particles. Nano Lett 3:1087–1090
8. Liu Y, Zentgraf T, Bartal G, Zhang X (2010) Transformational plasmon optics. Nano Lett 10:1991–1997
9. Huidobro PA, Nesterov ML, Martin-Moreno L, Garcia-Vidal FJ (1985) Transformation optics for plasmonics. Nano Lett 10
10. Cao YWC, Jin RC, Mirkin CA (2002) Nanoparticles with Raman spectroscopic fingerprints for DNA and RNA detection, Science 297:1536
11. Moskovits M (1985) Surface-enhanced spectroscopy. Rev Mod Phys 57:783
12. Elghanian R, Storhoff JJ, Mucic RC, Letsinger RL, Mirkin CA (1997) Selective colorimetric detection of polynucleotides based on the distance-dependent optical properties of gold nanoparticles. Science 227:1078
13. Brongersma ML, Hartman JW, Atwater HA (2000) Electromagnetic energy transfer and switching in nanoparticle chain arrays below the diffraction limit. Phys Rev B 62:R16356
14. Ricard D, Roussignol P, Flytzanis C (1985) Surface-mediated enhancement of optical phase conjugation in metal colloids. Opt Lett 10:511
15. Novotny L, Bain RX, Xie XS (1997) Theory of nanometric optical tweezers. Phys Rev Lett 79:645
16. Miao X, Lin LY (2007) Large dielectrophoresis force and torque induced by localized surface plasmon resonance of Au array, nanoparticle. Opt Lett 32:295–297
17. Aizpurua J, Hanarp P, Sutherland DS, Kall M, Bryant GW, Garcia de Agajo FG (2003) Optical properties of gold nanorings. Phys Rev Lett 90:057401

18. Garcia de Abajo FJ (2007) Light scattering by particle and hole arrays. Rev Mod Phys 79:1267–1290
19. Barnes WL, Dereux A, Ebbesen TW (2003) Surface plasmon subwavelength optics. Nature 424:824–830
20. Engheta N (2007) Circuits with light at nanoscales: Optical nanocircuits inspired by metamaterials. Science 317:1698–1702
21. Genet C, Ebbesen TW (2007) Light in tiny holes. Nature 445:39–46
22. Andkjær J, Sigmund O (2011) Topology optimized low-contrast all-dielectric optical cloak. Appl Phys Lett 98:021112
23. Andkjær J, Mortensen NA, Sigmund O (1106) Towards all-dielectric, polarization-independent optical cloaks. Appl Phys Lett 100(10)
24. Fujii G, Watanabe H, Yamada T, Ueta T, Mizuno M (2013) Level set based topology optimization for optical cloaks. Appl Phys Lett 102:251106
25. Noghani MT, Samiei MHV (2013) Analysis and optimum design of hybrid plasmonic slab waveguides. Plasmonics 8:1155–1168
26. Pellegrini G, Mattei G (2014) High-performance magneto-optic surface plasmon resonance sensor design: an optimization approach. Plasmonics. doi:10.1007/s11468-014-9764-6.
27. Wang H, An Z, Qu C, Xiao S, Zhou L, Komiyama S, Lu W, Shen X, Chu PK (2011) Optimization of optoelectronic plasmonic structures. Plasmonics 6:319–325
28. Andkjær J, Nishiwaki S, Nomura T, Sigmund O (2010) Topology optimization of grating couplers for the efficient excitation of surface plasmons. J Opt Soc Am B 27:1828–1832
29. Bendsoe MP, Sigmund O (2003) Topology optimization—theory, methods and applications. Springer, Berlin
30. Borrvall T, Petersson J (2003) Topology optimization of fluid in Stokes flow. Int J Numer Meth Fluids 41:77–107
31. Nomura T, Sato K, Taguchi K, Kashiwa T, Nishiwaki S (2007) Structural topology optimization for the design of broadband dielectric resonator antennas using the finite difference time domain technique. Int J Numer Meth Engng 71:1261–1296
32. Sigmund O, Hougaard KG (2008) Geometric properties of optimal photonic crystals. Phys Rev Lett 100:153904
33. Duhring MB, Jensen JS, Sigmund O (2008) Acoustic design by topology optimization. J. Sound Vibration 317:557–575
34. Akl W, El-Sabbagh A, Al-Mitani K (2008) Topology optimization of a plate coupled with acoustic cavity. Int J Solids Struct 46:2060–2074
35. Gersborg-Hansen A, Bendsoe MP, Sigmund O (2006) Topology optimization of heat conduction problems using the finite volume method. Struct Multidisc Optim 31:251–259
36. Zhou S, Li W, Sun G, Li Q (2010) A level-set procedure for the design of electromagnetic metamaterials. Optics Express 18:6693–6702
37. Zhou S, Li W, Chen Y, Sun G, Li Q (2011) Topology optimization for negative permeability metamaterials using level-set algorithm. Acta Materialia 59:2624–2636
38. Otomori M, Yamada T, Izui K, Nishiwaki S, Andkjær J (2012) A topology optimization method based on the level set method for the design of negative permeability dielectric metamaterials . Comput Methods Appl Mech Engrg 237-240:192–211
39. Sigmund O (1996) Materials with prescribed constitutive parameters: an inverse homogenization problem. Int J Solids and Struct 31:2313–2329
40. Deng Y, Liu Z, Zhang P, Liu Y, Wu Y (2011) Topology optimization of unsteady incompressible Navier-Stokes flows. J Comput Phys 230:6688–6708
41. Deng Y, Liu Z, Wu J, Wu Y (2013) Topology optimization of steady Navier-Stokes flow with body force. Comput Methods Appl Mech Eng 255:306–321
42. Deng Y, Liu Z, Liu Y, Wu Y (2014) Combination of topology optimization and optimal control method. J Comput Phys 257:374–399
43. Lazarov B, Sigmund O (2010) Filters in topology optimization based on Helmholtz type differential equations. Int J Numer Methods Eng. doi:10.1002/nme.3072
44. Jin J (2002) The finite element method in electromagnetics. Wiley, New York
45. Wang F, Lazarov BS, Sigmund O (2011) On projection methods, convergence and robust formulations in topology optimization. Struct Multidisc Optim 43:767–84
46. Xu S, Cai Y, Cheng G (2010) Volume preserving nonlinear density filter based on heaviside funtions. Struct Multidisc Optim 41:495–505
47. Guest J, Prevost J, Belytschko T (2004) Achieving minimum length scale in topology optimization using nodal design variables and projection functions. Int J Numer Methods Eng 61:238–254
48. Sigmund O (2007) Morphology-based black and white filters for topology optimization. Struct Multidisc Optim 33:401–424
49. Kawamoto A, Matsumori T, Yamasaki S, Nomura T, Kondoh T, Nishiwaki S. (2010) Heaviside projection based topology optimization by a pde-filtered scalar function. Struct Multidisc Optim. doi:10.1007/s00158-010-0562-2
50. Diaz AR, Sigmund O (2010) A topology optimization method for design of negative permeability metamaterials. Suct Multidisc Optim 41:163–177
51. Johnson PB, Christy RW (1972) Optical Constants of the Noble Metals. Phys. Rev. B 6:4370–4379
52. Hinze M, Pinnau R, Ulbrich M, Ulbrich S (2009) Optimization with PDE constraints. Springer, Berlin
53. Giles MB, Pierce NA (2000) An introduction to the adjoint approach to design. Flow, Turbulence and Combustion 65:393–415
54. Mohammadi B (2010) Pironneau O. Applied shape optimization for fluids OXFORD
55. Svanberg K (1987) The method of moving asymptotes: a new method for structural optimization. Int J Numer Meth Engng 24:359–373
56. http://www.comsol.com
57. Olesen LB, Okkels F, Bruus H (2006) A high-level programming-language implementation of topology optimization applied to flow, steady-state Navier-Stokes. Int J Numer Meth Engng 65:975–1001
58. Liu H, Lalanne P (2008) Microscopic theory of the extraordinary optical transmission. Nature 452:728–731
59. Garcia de Abajo FJ (2007) Light scattering by particle and hole arrays. Rev Modern Phys 79:1267–1290
60. Sødergaard T, Bozhevolnyi SI, Novikov SM, Beermann J, Devaux E, Ebbesen TW (2010) Extraordinary optical transmission enhanced by nanofocusing. Nano Lett 10:3123–3128
61. Liu H, Li T, Wang QJ, Zhu ZH, Wang SM, Li JQ, Zhu SN, Zhu YY, Zhang X (2009) Extraordinary optical transmission induced by excitation of a magnetic plasmon propagation mode in a diatomic chain of slit-hole resonators. Phys Rev B 79:024–304
62. García-Vidal FJ, Lezec HJ, Ebbesen TW, Martín-Moreno L (2003) Multiple paths to enhance optical transmission through a single subwavelength slit. Phys Rev Lett 90:213–901
63. Wang LL, Ren XF, Yang R, Guo GC, Guo GP (2009) Transmission of doughnut light through a bulls eye structure. Appl Phys Lett 95:111111–111113
64. Cui YX, He S, Okuno Y (2008) Giant optical transmission through a metallic nanoslit achieved by the optimization of the groove periodicity and other parameters. IEEE

65. Popov E, Nevière M, Fehrembach AL, Bonod N (2005) Optimization of plasmon excitation at structured apertures. Apploed Optics 44:6141–6154
66. Sorger VJ, Oulton RF, Yao J, Bartal G, Zhang X (2009) Plasmonic Fabry-Pérot Nanocavity. Nano Letters 9-10:3489–3493
67. Astilean S, Lalanne P, Palamaru M (2000) Light transmission through metallic channels much smaller than the wavelength. Opt Commun 175:265–273
68. Takakura Y (2001) Optical resonance in a narrow slit in a thick metallic screen. Phys Rev Lett 86:5601–5603
69. Yang F, Sambles JR (2002) Resonant transmission of microwaves through a narrow metallic slit. Phys Rev Lett 89:063901
70. Cai L, Li G, Wang Z, Xu A (2010) Interference and horizontal Fabry-Pérot resonance on extraordinary transmission through a metallic nanoslit surrounded by grooves. Opt Lett 35:127–129
71. Pendry JB, Schurig D, Smith DR (2006) Controlling electromagnetic fields. Science 312:1780
72. Leonhardt U (2006) Optical conformal mapping. Science 312:1777